AIAA JOURNAL
Vol. 47, No. 11, November 2009

Numerical Analysis of Three-Dimensional Flow of Supercritical Fluid in Asymmetrically Heated Channels

Marco Pizzarelli,* Francesco Nasuti,† Renato Paciorri,‡ and Marcello Onofri§
University of Rome "La Sapienza," 00185 Rome, Italy

DOI: 10.2514/1.38542

The knowledge of the flow behavior inside asymmetrically heated channels is of great importance to improve design and performance of regeneratively cooled rocket engines. The modeling of the coolant flow is a challenging task because of its particular features, such as the high wall temperature gradient, the high Reynolds number, the three-dimensional geometry of the passages, and the possible supercritical conditions of the fluid. In the present work, a numerical approach to study the turbulent flow of supercritical fluids is presented and validated by comparison with experimental data. Solutions of the supercritical nitrogen flowfield in an asymmetrically heated three-dimensional channel with a high-aspect ratio (channel height-to-width ratio) are presented and discussed. Emphasis is given to the analysis of the peculiar behavior and cooling performance of the supercritical fluid as compared with perfect gas. In particular, a long channel is considered, such that entrance effects are negligible, to analyze in detail wall heat-flux evolution throughout the channel.

Nomenclature

A	=	cross-sectional area
a	=	speed of sound
B	=	channel width
c_p	=	specific heat at constant pressure
c_v	=	specific heat at constant volume
D_h	=	hydraulic diameter
E	=	total energy per unit volume
e	=	internal energy
$\mathbf{F_j}$	=	vector of Eulerian fluxes
f_w	=	skin-friction coefficient
$\mathbf{G_j}$	=	vector of viscous fluxes
H	=	channel height
h	=	enthalpy
k	=	thermal conductivity
L	=	channel length
m	=	mass
$\dot{m}$	=	mass flow rate
Nu	=	Nusselt number
$\mathbf{n}$	=	unit vector normal to the control surface
P	=	cross-sectional perimeter
Pr	=	Prandtl number
p	=	pressure
Q	=	fluid energy
$\dot{Q}$	=	heat transfer rate
q	=	heat flux
R	=	perfect gas constant
Re	=	Reynolds number
$\mathcal{S}$	=	control surface
s	=	entropy
T	=	temperature
t	=	time
$\mathbf{U}$	=	vector of conserved variables
u	=	velocity
$\mathcal{V}$	=	control volume
v	=	specific volume
x, y, and z	=	length, width, and height coordinates
y^+	=	nondimensional wall distance
Z	=	compressibility factor
α, β, and γ	=	modified Benedict–Webb–Rubin equation of state coefficients
ε	=	thermal energy absorbed by the coolant per unit length and mass
μ	=	viscosity
ρ	=	density
τ_{ij}	=	stress tensor

Subscripts

b	=	bulk
c	=	critical value
e	=	exit
i	=	inlet
r	=	reference value
w	=	wall
0	=	stagnation value

Presented as Paper 5501 at the 43rd AIAA/ASME/SAE/ASEE Joint Propulsion Conference and Exhibit, Cincinnati, OH, 8–11 July 2007; received 13 May 2008; revision received 24 September 2008; accepted for publication 25 June 2009.

*Research Fellow, Department of Mechanics and Aeronautics, Via Eudossiana 18. Member AIAA.

†Associate Professor, Department of Mechanics and Aeronautics, Via Eudossiana 18. Senior Member AIAA.

‡Associate Professor, Department of Mechanics and Aeronautics, Via Eudossiana 18.

§Professor, Department of Mechanics and Aeronautics, Via Eudossiana 18. Senior Member AIAA.

I. Introduction

TO AVOID thermal failure in high-pressure thrust chambers of liquid rocket engines, a regenerative cooling system is generally considered. In this system, one of the propellants (typically the fuel) is forced through passages that are machined inside the thrust chamber wall, then is injected into the thrust chamber or goes to the turbine. The thermal analysis is a major issue in the design of a liquid rocket engine, because the prediction of the peak heat flux from the combustion gases to the engine wall is necessary to ensure the structural integrity of the combustion chamber. The need for thermal analysis is especially important in reusable engines (in which an effective and efficient cooling system is crucial to extend the engine life) or in expander cycle engines (in which coolant warming provides the available power for turbomachinery).

Thermal and fluid-dynamic analysis of coolant flow definitely becomes important if the goal is to search for a more efficient cooling

channel configuration such as that of rectangular channels with a high-aspect ratio (channel height-to-width ratio), often referred to as HARCC (high-aspect ratio cooling channels) [1,2]. In this case, the wall temperature is reduced by increasing the coolant side surface area (relative to the hot gas side surface) by the use of extended fins (Fig. 1). Increasing the surface area of the cooling passages necessarily increases their aspect ratio. In this case, the flow in the cooling channels is strongly three-dimensional (3-D) [2,3] and the resulting temperature stratification in the radial direction strongly influences the heat transfer efficiency of the coolant [3]. A further modeling complication is that the coolant might be neither a perfect gas nor an incompressible fluid. In fact, in these systems, the large pressure required in the combustion chamber is sufficient to ensure that some coolant remain supercritical (i.e., pressure over the critical point; for instance, this is the case of hydrogen and methane) along the entire length of the cooling passages, as it moves from a predominantly liquidlike regime (weakly compressible flow) at the manifold inlet to a predominantly gaseouslike regime (highly compressible flow) at the chamber injectors or turbine; therefore, the methods based on the assumption of perfect gas or incompressible fluid cannot be used [4,5].

For this reason, since the early 1990s, many researchers have studied 3-D flow of supercritical fluids in cooling channels using appropriate Navier–Stokes solvers [2,4–9]. To simplify the problem and avoid time-consuming computations, low Reynolds number duct flows without the coupling between the coolant flow and the wall thermal conduction were analyzed first. These studies have qualitatively shown the importance of 3-D phenomena in cooling passages. Then, more recently, because of the practical interest in the design of high-performance combustion chambers, with particular regard to the cryogenic expander cycle engines, new computations have been presented, some of which include coupled studies of 3-D coolant flow and wall thermal analysis [6,7,10]. However, in spite of the massive computer power used, due to the actual channel flow conditions (Reynolds number up to 10^7 and strong wall temperature gradient), the studies of the detailed flowfield mechanism that control heat transfer in HARCC are still under way [8].

With the final aim of simulating rocket HARCC flows, the objective of this paper is to present and validate a numerical approach to solve Reynolds-averaged Navier–Stokes equations for a generic real fluid and discuss some of the most peculiar aspects of the flow of an asymmetrically heated supercritical fluid as compared with the behavior of a perfect gas. In particular, validation by simulation of heated nitrogen flow in a straight circular tube and simulation of nitrogen flow in long straight 3-D channels with wall temperature gradients and a high-aspect ratio of the cross section will be presented and discussed, with emphasis devoted to the evolution of heat flux and bulk temperature throughout the channel.

II. Physical Model

Suitable physical modeling has to be considered to describe the fluid dynamics that occur in some peculiar technological systems in which fluid is supercritical. In fact, in the case of supercritical pressure, the thermodynamic behavior of the fluid is not described by a perfect gas or incompressible fluid equation of state (EOS). Its behavior is similar to that of a compressible liquid, in the sense that its density is similar to that of a liquid but its compressibility is nonzero. Moreover, in the supercritical region, the fluid properties are strongly dependent on both temperature and pressure [11].

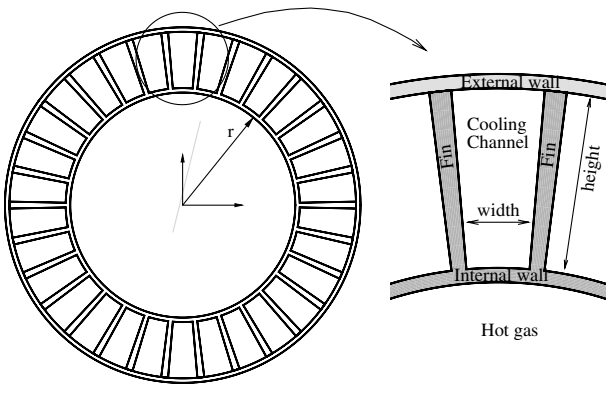

Fig. 1 Schematic of cooling-channels geometry.

To study the flow of a supercritical fluid, it is therefore necessary to consider a nonstandard model able to deal with a more generic fluid than perfect gas or incompressible fluid. In particular, for the applications of interest in this paper, the attention can be limited to a single-phase compressible fluid. A compressible fluid is such to satisfy the condition

$$\left(\frac{\partial v}{\partial p}\right)_s < 0 \tag{1}$$

The previous condition, as a matter of fact, is valid for all single-phase fluids but the incompressible fluids, for which the EOS is $v = \text{const}$. For this reason, incompressible fluids show compressibility equal to zero, and thus speed of sound, which tends to infinity. However, these fluids are only an idealization of liquids or dense fluids, which always exhibit a finite compressibility.

In the case of compressible fluid, the integral governing equations are the Reynolds-averaged Navier–Stokes equations (that is, mass, momentum, and energy equations) that can be written in conservative form for a fixed volume $\mathcal{V}$ (bounded by a surface $\mathcal{S}$), in a Cartesian frame of reference, as follows:

$$\frac{\mathrm{d}}{\mathrm{d}t}\int_V \boldsymbol{U}\,\mathrm{d}V + \oint_{\mathcal{S}} \sum_{j=1}^{3} \boldsymbol{F_j} n_j\,\mathrm{d}\mathcal{S} = \oint_{\mathcal{S}} \sum_{j=1}^{3} \boldsymbol{G_j} n_j\,\mathrm{d}\mathcal{S} \tag{2}$$

In the previous equation, $\boldsymbol{U}$ is the vector of conserved variables, $\boldsymbol{F_j}$ is the vector of the Eulerian fluxes, and $\boldsymbol{G_j}$ is the vector of viscous fluxes:

$$\boldsymbol{U} = \begin{pmatrix} \rho \\ \rho u_1 \\ \rho u_2 \\ \rho u_3 \\ E \end{pmatrix}; \qquad \boldsymbol{F_j} = \begin{pmatrix} \rho u_j \\ \rho u_1 u_j + p\delta_{1j} \\ \rho u_2 u_j + p\delta_{2j} \\ \rho u_3 u_j + p\delta_{3j} \\ (E+p)u_j \end{pmatrix}$$

$$\boldsymbol{G_j} = \begin{pmatrix} 0 \\ \tau_{1j} \\ \tau_{2j} \\ \tau_{3j} \\ \sum_{i=1}^{3} \tau_{ij} u_i - q_j \end{pmatrix}; \qquad (j = 1, 2, 3) \tag{3}$$

where ρ is the density of the fluid, p is the pressure, u_i is the ith component of the velocity,

$$E = \rho\left(e + \sum_{i=1}^{3} \frac{1}{2} u_i u_i\right)$$

is the total energy per unit volume, e is the specific internal energy, τ_{ij} is the viscous molecular or turbulent stress tensor, q_j is the jth component of the vector of molecular or turbulent heat flux, n_j is the jth component of the outward-facing unit vector orthogonal to the surface $\mathcal{S}$, and δ_{ij} is the Kronecker delta. The molecular part of the stress tensor has been modeled as a general Newtonian fluid and the heat flux by the Fourier's law, whereas the turbulent part of the stress tensor and heat-flux vector have been modeled according to the Spalart–Allmaras turbulence model [12].

The system of the governing equations (2) is written without any characterization upon the thermodynamic behavior of the fluid, that is, without any characterization of the EOS and the modeling of transport properties that are necessary for the solution. However, the range of fluids of interest is limited here to the case of compressible fluids with convex EOS. A fluid with convex EOS is such to satisfy the condition

$$\left(\frac{\partial^2 v}{\partial p^2}\right)_s > 0 \tag{4}$$

This condition assures that the considered flowfield is based on the classical fluid dynamics: the expansion wave is an isentropic wave, and the shock wave is a nonisentropic compression wave [13]. Equation (4) is valid for all but the Bethe–Zel'dovich–Thompson fluids [14] that present a nonconvex behavior in the vicinity of the saturated vapor region (typically, this is the case for high molecular-weight fluorocarbons and hydrocarbons).

Among the proposed EOS for supercritical fluids, the modified Benedict–Webb–Rubin (MBWR) equation [15] has been selected because it shows high precision to determine the correct thermodynamic behavior for the fluids of interest in the present paper. The MBWR EOS is:

$$p(\rho, T) = \sum_{i=1}^{9} \alpha_i(T)\rho^i + \exp(-\gamma\rho^2) \sum_{j=1}^{6} \beta_j(T)\rho^{2j+1} \tag{5}$$

where γ is a constant coefficient and $\alpha_i(T)$ and $\beta_j(T)$ are simple functions of temperature determined by a total of 32 parameters (for which the values, computed by least-squares interpolation of empirical data, are taken from [15]). The MBWR EOS, together with a proper modeling of perfect gas specific heat, is also used to compute the thermodynamic properties of the fluid. In fact, enthalpy, specific heats, and the speed of sound of a generic fluid can be expressed as:

$$h(\rho, T) = h_r + \frac{p - \rho RT}{\rho} + \int_{T_r}^{T} c_{pr}(T)\,\mathrm{d}T + \int_0^{\rho} \left[\frac{p}{\rho^2} - \frac{T}{\rho^2}\left(\frac{\partial p}{\partial T}\right)_\rho\right]_T \mathrm{d}\rho \tag{6}$$

$$c_v(\rho, T) = c_{pr}(T_r) - R - \int_0^{\rho} \left[\frac{T}{\rho^2}\left(\frac{\partial^2 p}{\partial T^2}\right)_\rho\right]_T \mathrm{d}\rho \tag{7}$$

$$c_p(\rho, T) = c_v(\rho, T) + \frac{T}{\rho^2}\left[\left(\frac{\partial p}{\partial T}\right)_\rho^2 \Big/ \left(\frac{\partial p}{\partial \rho}\right)_T\right] \tag{8}$$

$$a(\rho, T) = \sqrt{\frac{c_p}{c_v}\left(\frac{\partial p}{\partial \rho}\right)_T} \tag{9}$$

where $c_{pr}(T)$ (for which the modeling is also taken from [15]) is the perfect gas specific heat at constant pressure (which is a function of temperature only) and T_r, p_r, and $h_r = h_r(T_r)$ are the perfect gas reference variables. Note that Eqs. (6–9) can be computed analytically by differentiating the MBWR EOS with respect to temperature and density and then integrating the resulting integrals in Eqs. (6) and (7). The remaining relations necessary to describe the thermodynamic behavior of the fluid are those for viscosity and thermal conductivity:

$$\mu = \mu(\rho, T) \tag{10}$$

$$k = k(\rho, T) \tag{11}$$

which are also taken from [15].

As an example of real fluid, the behavior of nitrogen (which is the fluid considered in the present study) is computed by the MBWR EOS and is shown by isodensity lines on the pressure–temperature state diagram in Fig. 2a. In this diagram, the critical point (identified by pressure $p_c = 33.99$ bar and temperature $T_c = 126.26$ K) is clearly visible, because above critical pressure, the phase change does not occur and density variation with temperature, although strong, is continuous: the density ranges from 850 kg/m^3 in the low-temperature liquidlike region to 20 kg/m^3 in the high-temperature gaslike region. Many other thermodynamic variables change dramatically in the case of supercritical pressure, such as the specific heat at constant pressure, the speed of sound, the viscosity, and the thermal conductivity. In Fig. 2b, the nitrogen isentropic lines in the pressure–volume state diagram are shown. Note that, as these lines have negative slope and are convex, nitrogen satisfies both conditions (1) and (4). Isentropes in the two-phase region (the blank zone in Fig. 2b) are not shown because only single-phase fluids are considered in the present study.

III. Numerical Method

As the fluid is compressible, the convective part of the governing equations (that is, Eqs. (2) with $\boldsymbol{G}_j = \boldsymbol{0}$) is hyperbolic and thus a numerical scheme based on wave propagation can be adopted [16]. In particular, the numerical solution of the governing Eqs. (2) is carried out by a time-dependent gas dynamics solver, which is based on a Godunov-type finite volume method [17,18]. According to the previously mentioned cell-centered finite volume method, the fluid domain is divided into control volumes and, for the generic hexahedral control volume, the governing equations are written as

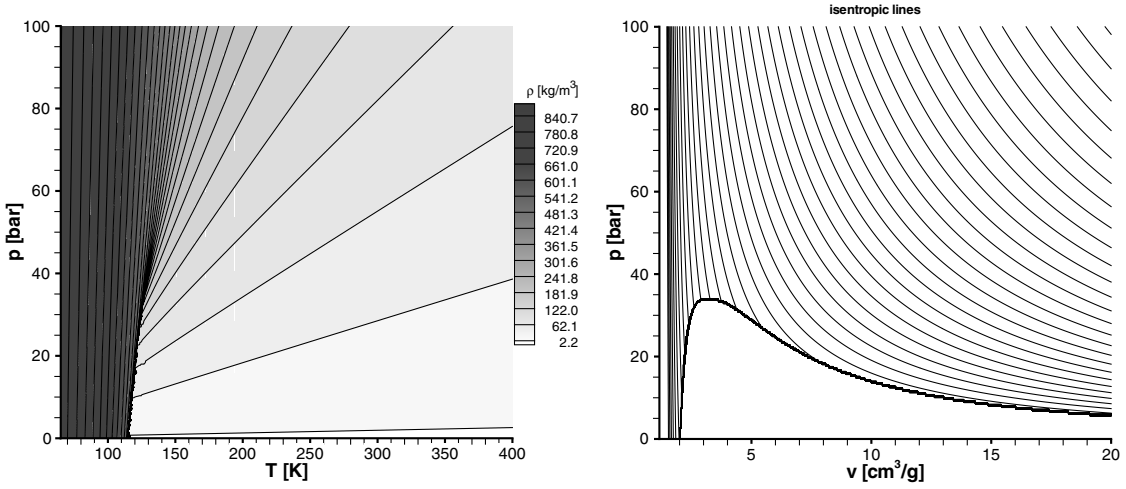

a) Nitrogen density behavior on a pressure-temperature state diagram

b) Nitrogen isentropes behavior on a pressure-volume state diagram

Fig. 2 Nitrogen state diagrams [according to Eq. (5)].

$$\left(\frac{\mathrm{d}\bar{\boldsymbol{U}}}{\mathrm{d}t}\right)\mathcal{V}+\sum_{k=1}^{6}\sum_{j=1}^{3}\tilde{\boldsymbol{F}}_j^k n_j^k \mathcal{S}^k=\sum_{k=1}^{6}\sum_{j=1}^{3}\tilde{\boldsymbol{G}}_j^k n_j^k \mathcal{S}^k \tag{12}$$

where the k summation is over all six faces of the control volume. The overbar indicates the average value of the conserved variables in the control volume and the tilde indicates the numerical flux (Eulerian and viscous) through face $\mathcal{S}^k$. To obtain second-order-accuracy in space, the viscous fluxes are evaluated by second-order-accurate central differencing, whereas the Eulerian fluxes are evaluated by the solution of a Riemann problem at the cell interfaces and by linear cell reconstruction of primitive variables using a minmod slope limiter to satisfy the total variation diminishing-stability condition. In this scheme, an approximate solution of the Riemann problem was used; note that the convex behavior [Eq. (4)] of the present real fluids assures that the waves originated from a Riemann problem are the same as perfect gas [16]. For this reason, the extension of a perfect gas Riemann solver to real fluids is rather straightforward [19], and thus it is omitted here. To avoid time-consuming computations, a primitive variable Riemann solver (PVRS) [20] has been implemented to evaluate the Eulerian fluxes. Unlike the exact Riemann solver or other approximate solvers (such as the Roe solver [21]), the PVRS requires a minimum number of computations of the thermodynamic fluid properties. In fact, the PVRS provides the solution of the Riemann problem in a linearized form of the Euler equation, written with respect to the primitive variables (i.e., density, velocity, and pressure). According to numerical tests carried out in the present study, the PVRS solver is as much as 50% faster than the Roe solver and 80% faster than the Harten–Lax–van Leer [20] and Harten–Lax–van Leer–contact [20] solvers. This result, which is mainly due to the minimum number of the EOS computations requested, has led to the choice of PVRS, because the solver affects in a minor way the computational fluid dynamics (CFD) solution of viscous flowfields without strong fluid-dynamic discontinuities [20], such as those of interest in the present study. The final results of the discretization of Eulerian and viscous fluxes is a scheme that, if the solution is smooth enough, is second-order-accurate in space.

Steady-state solution is reached by carrying out time integration until the mass equation residual, which is based on the flowfield density variation between two consecutive time steps, is reduced by a reasonable quantity (6 to 8 orders of magnitude generally suffices to reach steady state). To speed up convergence to steady state, a local time step is used.

The conservative formulation of the governing equations (2) and (3) makes it convenient to write the following generic EOS and the other thermodynamic properties in terms of ρ and p as the independent thermodynamic variables:

$$\begin{aligned} &T=T(\rho,p); \qquad c_p=c_p(\rho,p); \qquad a=a(\rho,p)\\ &e=e(\rho,p); \qquad \mu=\mu(\rho,p); \qquad k=k(\rho,p) \end{aligned} \tag{13}$$

This is not a limitation, because all fluids of interest can be modeled in that way, but it requires the time-consuming inversion of the expressions (5–11). Therefore, the computations necessary to obtain the thermodynamic properties [as shown in Eq. (13)] are made once for all, and the results are stored in a discrete database. As a consequence, the complexity of the selected EOS does not affect the computational cost of the gas dynamic solver, because the thermodynamic database computation is made apart from the CFD computations. The database is based on regular discretization Δp and $\Delta\rho$, and Eqs. (13) are computed by bilinear interpolation. This approach obtains the desired value without any iterative searching algorithm; high accuracy is obtained by reducing pressure and density discretization steps, because the error of the discretization is governed by Δp^2 and $\Delta\rho^2$. Note that the discretization of the thermodynamic properties must be performed efficiently and accurately because, in supercritical conditions, fluid properties change dramatically even for small density and pressure variations. The nitrogen database used in the present study is characterized by $\Delta p = 0.1$ bar and $\Delta\rho = 0.2$ kg/m^3 as a result of a compromise between computational cost and accuracy; the estimated error of the selected database is much lower than 0.01% in the present thermodynamic range of interest.

Table 1 Boundary conditions for the CFD test cases

Parameter	TC1	TC2	TC3
$T_{0,i}$, K	280.6	280.6	280.7
$p_{0,i}$, bar	49	50	53
p_e, bar	48	48	48
q_w, MW/m^2	0.84	0.3	0.3

IV. Validation

Only a few data are available in the open literature for the validation of the present numerical model. Among them, the experimental results provided in [22] for the flow in an axisymmetrically heated straight tube with a circular cross section have been selected. The considered coolant is the supercritical nitrogen at an inlet temperature of 280 K and inlet pressure of up to 100 bar. The straight tube has a length of 432 mm and an internal diameter of 5.64 mm, and it is electrically heated to provide nearly constant heat flux along the channel length. Test conditions considered in [22] are relevant to the different values of pressure, Reynolds number, and entering wall heat flux, and they provide heat transfer data for a fluid weakly different from perfect gas. In particular, the relatively high Reynolds number of the flow (of the order of 10^6) and the entering heat flux (of the order of 10^6 W/m^2) make the selected experimental results a proper test case to validate the present numerical model, which is aimed to turbulent heated flows.

To validate the present numerical approach, three numerical test cases (which will be referred to as TC1, TC2, and TC3, respectively) have been carried out to reproduce the entire Nusselt and Reynolds number ranges of the experimental data. The channel dimensions are those of the experimental device, and the supercritical nitrogen thermodynamic properties are taken from [15]. The boundary conditions of the computed test cases are summarized in Table 1: total temperature and pressure are enforced at inflow, static pressure is enforced at outflow, and no-slip flow with assigned heat flux is enforced at the wall; symmetry conditions on the side faces of the slice of channel are considered because of axisymmetry. The CFD solutions of the three selected test cases have been verified by a grid convergence analysis that has been performed on three grid levels. The fine grid has 96 cells in the streamwise direction and 64 cells in the crosswise direction, the medium grid has 48×32 cells, and the coarse grid has 24×16 cells. Each mesh coarsening has been

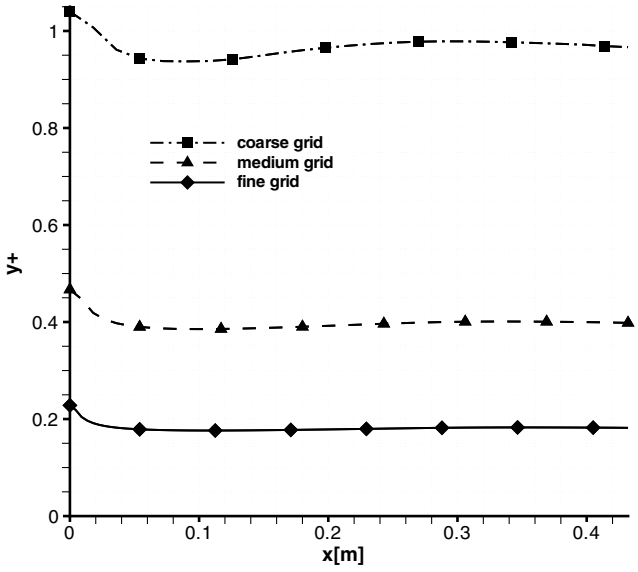

Fig. 3 Profile of y^+ at a wall-adjacent cell, along the channel length, and for the three grid refinements (TC2).

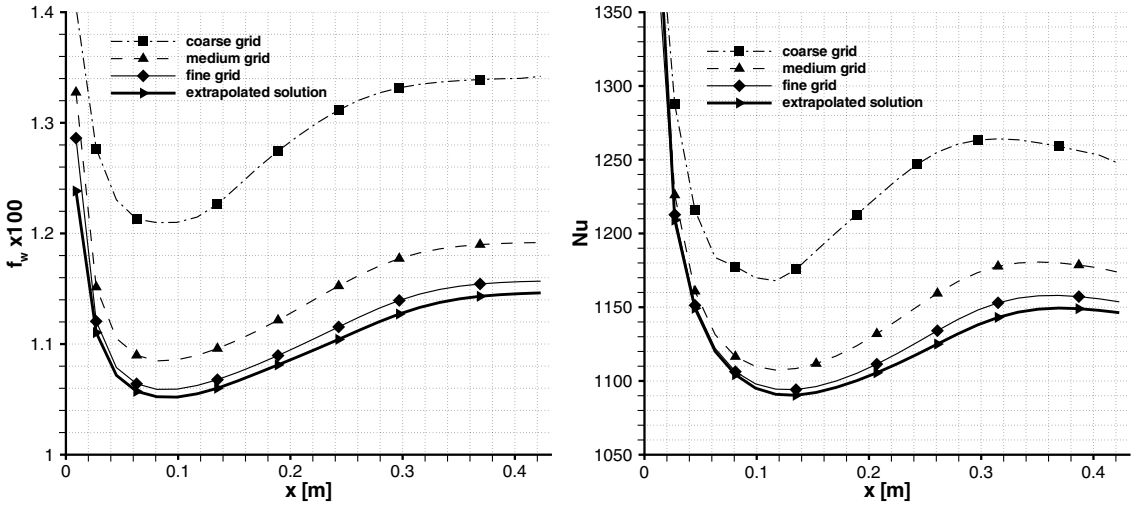

a) Skin friction coefficient **b) Nusselt number**

Fig. 4 CFD solutions of TC2 obtained with different grid refinements.

obtained by removing one node out of two in each coordinate direction of the finer mesh. Note that cells are clustered toward the walls to accurately describe the turbulent boundary layers. In Fig. 3, the value of the y^+ parameter at wall-adjacent cell is presented for the three grid levels. This nondimensional parameter, which is an indication of the mesh spacing close to the wall, is below the unity for all grid refinements (as demanded by the Spalart–Allmaras turbulence model to describe the laminar sublayer).

The convergence behavior for the skin-friction coefficient and the Nusselt number are presented in Fig. 4, in which the coarse, medium, and fine grid solutions of TC2 are plotted, as well as the extrapolated solution computed by means of the Richardson method [23]. Figure 4 qualitatively shows the asymptotic grid convergence of the numerical solution, with fine-grid solutions very close to extrapolated ones. In particular, the maximum numerical error of the skin-friction coefficient, with respect to the extrapolated solution, is 1.1% for the fine-grid solution and 4.4% for the medium-grid solution. In the case of the Nusselt number, the maximum error is almost the same: 0.9% for the fine-grid and 3.2% for the medium grid. On the other hand, the quantitative analysis of solutions obtained on three grid levels confirms that the spatial order of accuracy, computed on the skin-friction coefficient and the Nusselt number (and sufficiently far from the channel inlet), is close to the formal value (the scheme is second-order-accurate in space). This confirms the asymptotic behavior of the numerical error and thus gives a good confidence on the error estimate. The CFD solutions obtained by the three grid refinements and their extrapolation for the skin-friction coefficient and the Nusselt number close to the channel exit are also reported, together with the spatial order of accuracy (computed by means of the Richardson method [23]) for the sake of clarity in Table 2. A quite similar grid convergence behavior has been verified for TC1 and TC3.

Experimental heat transfer data are presented in [22] as a plot of the experimental Nusselt number Nu versus the value of the Nusselt number predicted by a modified version of Taylor's model Nu_{Taylor} (Fig. 5). The latter value is obtained by the formula [22]

Table 2 Grid convergence analysis of TC2 for the skin-friction coefficient and the Nusselt number at channel section $x = 405$ mm

	$f_w \times 100$	Nu
Coarse grid	1.3402	1253.17
Medium grid	1.1915	1176.60
Fine grid	1.1564	1155.70
Extrapolation	1.1456	1147.86
Spatial order of accuracy	2.08	1.87

$$Nu_{\text{Taylor}} = 0.023 Re_b^{0.8} Pr_b^{0.4} \left(\frac{T_w}{T_b}\right)^{-0.3} \tag{14}$$

where the subscript b refers to bulk quantities, which are values computed by suitable averaging on tube cross sections. The modified Taylor's model is considered, as it provides a good estimation of the experimental results with an error lower than 10% [22]. Note that data reported in Fig. 5 refer only to the central portion of the tube to avoid entry and exit effects which are strongly connected to the experimental facility status. The numerical results are overprinted, for the sake of comparison, on Fig. 5, whereas the extrapolated solution of the Nusselt number is reported, for the three test cases, in Table 3. To compare the CFD results and the experimental data, the Nusselt number predicted by the modified Taylor's model is also presented in Table 3, together with the range that includes the experimental results. All numerical results fall in the range foreseen by the modified Taylor's model, showing a good agreement with the experimental data.

V. Results

A. Test Case

A 3-D straight-channel flow has been analyzed using the present CFD code. The fluid is again the supercritical nitrogen described as a fictitious thermally and calorically perfect gas and as a real fluid with

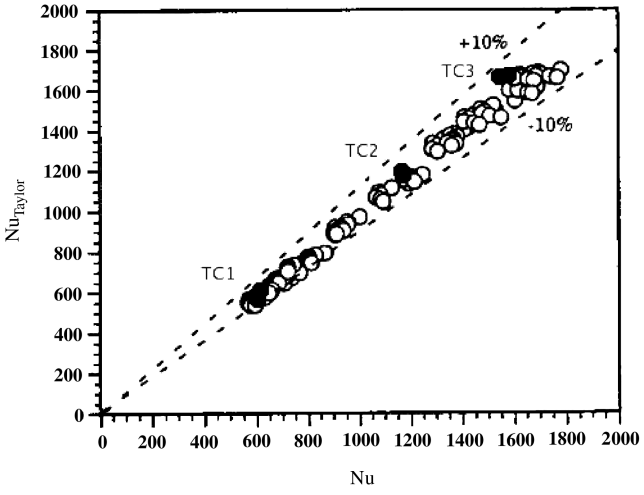

Fig. 5 Comparison of Nusselt numbers calculated with modified Taylor's equation to experimental data [22] (hollow circles) and present calculations (filled circles).

Table 3 Extrapolated solution of the Nusselt number provided by CFD and Taylor's model at channel section $x = 405$ mm

	Nu	$Nu_{\text{Taylor}} \pm 10\%$
TC1	579.57	559.84/684.24
TC2	1147.86	1090.61/1332.97
TC3	1537.01	1515.70/1852.521

properties given by the MBWR EOS (5) and with transport properties [Eqs. (10) and (11)] provided in [15]. In particular, the effect of the real fluid behavior in an asymmetrically heated rectangular channel has been studied and compared with that of perfect gas. The main features of the test case are a turbulent flow, a high-aspect ratio of the cross section, a nonuniform wall temperature distribution that induces fluid thermal stratification, and supercritical flow conditions. The dimensions of the channel have been selected so that the Reynolds number is approximately 60,000; as a consequence, the channel dimensions are quite small. Although the Reynolds number is much lower than in actual applications, the selected flow condition permits an affordable evaluation of the 3-D turbulent flowfield with asymmetric heating and comprehension of the basic phenomena (such as thermal stratification and wall heat-flux distribution) that occur in a full-scale channel. The channel has an aspect ratio of $H/B = 8$, where H is the height and B is the base of the cross section, nondimensional length $L/D_h = 168.75$, where D_h is the hydraulic diameter, and absolute dimensions $B = 0.1$ mm, $H = 0.8$ mm, and $L = 30$ mm (see Fig. 6). To study the flowfield of a fluid sufficiently different from the perfect gas, the inlet flow conditions are slightly over the critical point. In particular, the inlet stagnation temperature is $T_0 = 150$ K and the pressure is $p_0 = 45$ bar, whereas the outflow static pressure is $p_e = 40$ bar. The wall temperature is $T_w = 150$ K at the cold side (top wall) and $T_w = 300$ K at the hot side (bottom wall), and a linear distribution of temperature is considered on the side wall. Note that the wall temperature at the top wall is equal to the stagnation inlet temperature. Because the flow is symmetric with respect to the vertical centerplane, only one half of the physical domain is discretized, and a symmetric flow condition is imposed as the boundary condition on the channel centerplane.

B. Grid Convergence

The 3-D computational grid (composed by $40 \times 120 \times 60$ volumes in the base, height, and length directions, respectively) is clustered near the wall to accurately describe the turbulent boundary layer. To verify solutions by grid convergence analysis, a medium and a coarse grid, with respect to the previously mentioned fine grid, have been considered. The medium grid has $20 \times 60 \times 30$ volumes that have been obtained by removing one node out of two, in each coordinate direction, from the fine grid. In the same way, the coarse-grid volumes of $10 \times 30 \times 15$ have been obtained from the medium grid.

The streamwise velocity profiles of the real fluid, obtained at the channel exit with different grid refinements, are shown in Fig. 7. In particular, grid convergence analysis of streamwise velocity shows that the solution has reached the asymptotic grid convergence range, with the observed accuracy order being quite close to the formal one. The error for the fine-grid solution is therefore well estimated by means of the Richardson extrapolation [23] and is less than 0.4%.

The error analysis has also been made for the wall heat-flux distribution along the bottom and side walls. Heat-flux distribution obtained with different grid refinements, in the case of real fluid, is shown in Fig. 8. The results indicate that the solution is characterized by small numerical errors: the maximum error of wall heat flux provided by the fine-grid solution is less than 0.7%. The value of the y^+ parameter at the wall-adjacent cell is below unity for the medium and fine grids, and it is of order 1 for the coarse grid, proving that the laminar sublayer is accurately described (see Fig. 8).

The CFD solutions of wall heat flux (obtained by the three grid refinements) and their extrapolation, together with the spatial order of accuracy, are presented in Table 4 for the sake of clarity. In particular, the presented wall heat flux has been evaluated at the middle of the channel height $z = H/2$ and base $y = 0$.

C. Discussion

The peculiar 3-D behavior of the nitrogen flow is shown by temperature, density, compressibility factor, and streamwise velocity fields in Fig. 9. These plots show the evolution of the variables at different sections, which are located every 6 mm along the streamwise direction, from the inlet toward the exit. Each cross-sectional plot shows the perfect gas and the real fluid solutions on the two sides of the channel vertical symmetry plane: the perfect gas solution is on the left side and the real fluid solution is on the right side.

Nitrogen enters the channel with a low-temperature, high-pressure (i.e., high density) condition; in particular, the perfect gas enters the channel with a density of 100 kg/m^3, whereas the real fluid enters with a density of 145 kg/m^3 due to its lower compressibility factor. Then, it is heated up by the entering heat flux from the hot walls. As a consequence, the fluid accelerates while its pressure decreases, due

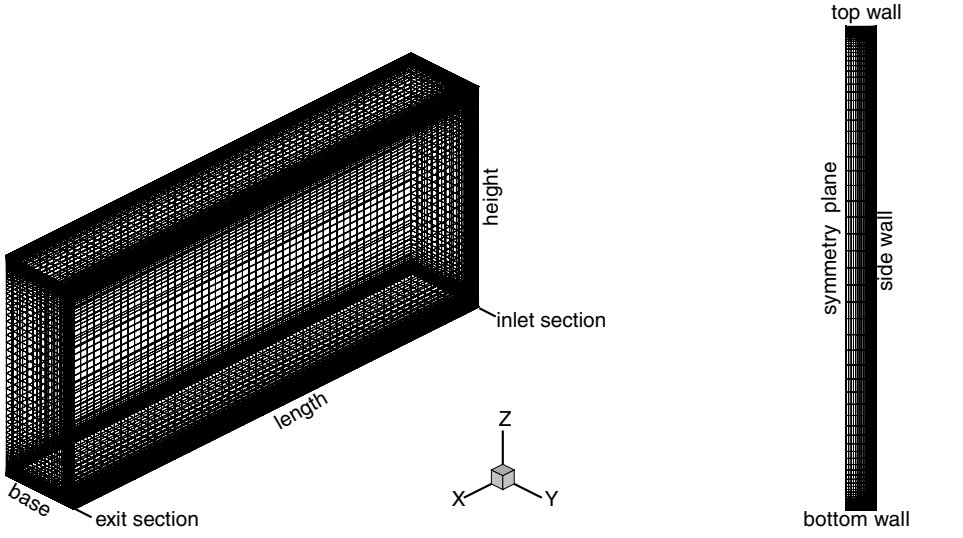

a) Three-dimensional mesh (the figure is not to scale)

b) Mesh view of the cross sectional plane

Fig. 6 Computational mesh (fine grid) of the 3-D channel.

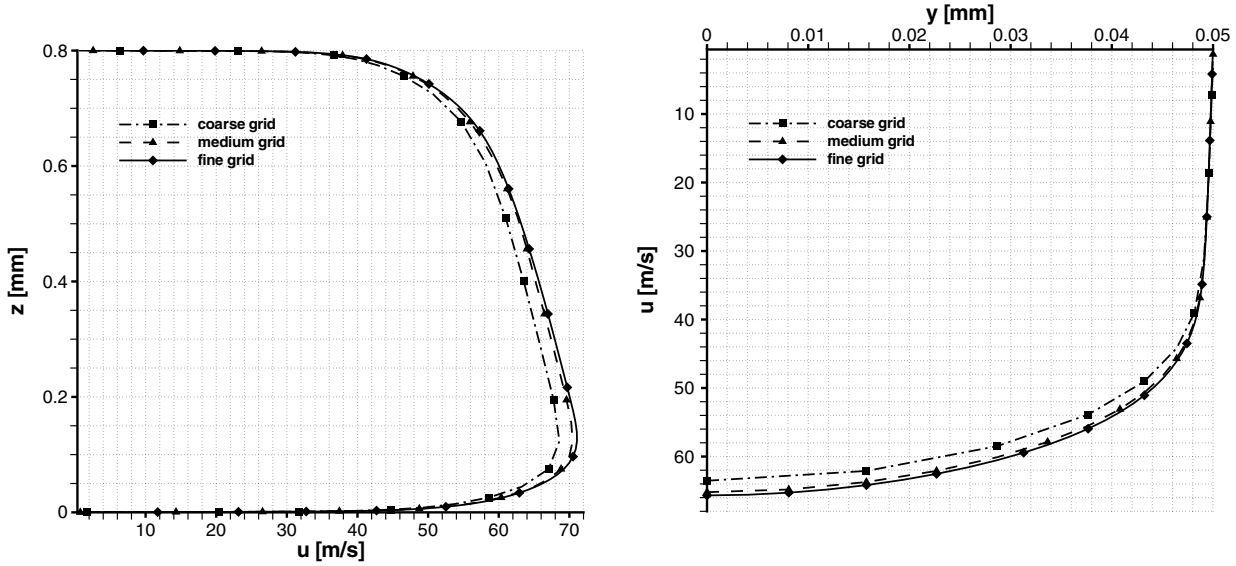

a) Vertical centerplane b) Horizontal centerplane

Fig. 7 Streamwise velocity profiles of real fluid (at the last channel section) obtained with different grid refinements.

to the friction force acting on the channel wall and the entering heat flux. The flowfield exhibits a pronounced asymmetric behavior because of the asymmetric wall temperature distribution and the 3-D geometry of the duct. However, for both the perfect gas and the real fluid, the pressure distribution is one-dimensionlike. Pressure variation in a generic cross section remains, in both cases, always within 0.01%. The one-dimensional behavior of pressure is a direct consequence of the straight-channel geometry with a constant cross section. Moreover, pressure loss is not strongly affected by the selected EOS. In fact, in the case of perfect gas, pressure loss is 3.99 bar, and in the case of real fluid, pressure loss is 4.13 bar. The small difference is due to the fact that both perfect gas and real fluid have the same pressure gradient $p_{0,i} - p_e$ as a boundary condition and that the skin friction (which is a function of the Reynolds number for smooth ducts) acts in both cases on the same channel surface.

Figure 9a shows the temperature stratification at different cross sections. As expected, the high-temperature flow region, induced by the hot-wall boundary condition, grows as the fluid moves from the inlet toward the exit section. In the last cross section, due to the long length of the channel, temperature stratification is almost the same as that imposed at the wall (linear temperature distribution). However, temperature evolution of the two fluids from the inlet to the exit section is rather different; due to the lower thermal diffusivity of the real fluid (mostly due to its higher density and specific heat), temperature diffusion across the channel cross section is less intense. The different thermal behavior of real fluid and perfect gas can be quantified by the Peclet number, which is the product of the Reynolds number and the Prandtl number. In fact, this dimensionless number relates the rate of advection of a flow to its rate of thermal diffusivity; hence, the lower the Peclet number, the larger the thermal diffusion in the cooling channel. The Peclet number of the real fluid can reach twice the value of that reached by the perfect gas. The different thermodynamic behavior of the two fluids also influences the shape of the temperature contour lines; in the case of real fluid, in fact, these lines are steeper.

The analysis of Fig. 9b shows the different density stratifications that occur in the two cases; the density variations (both in the streamwise direction and in the cross section) of the real fluid are much larger than in the perfect gas case. In fact, for a given supercritical pressure and temperature range, the higher density variation of the real fluid with respect to that of perfect gas is directly related to the different compressibility of the two fluids. In particular, even if the temperature and pressure distributions are quite similar in the exit section, the perfect gas density ranges from 45 to 90 $\mathrm{kg/m^3}$, whereas

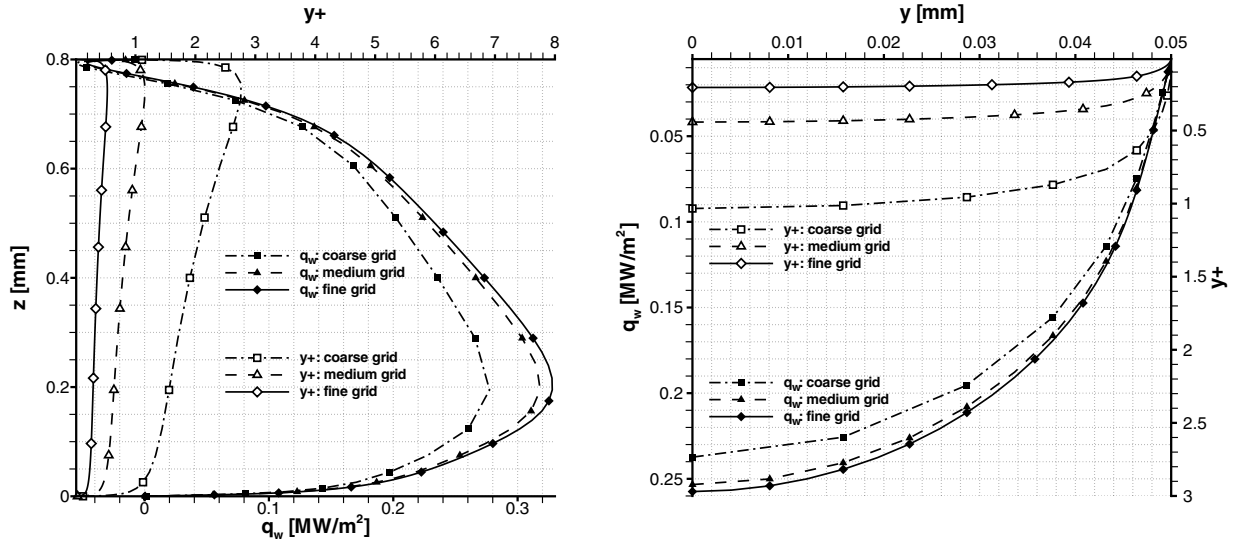

a) Side wall b) Bottom wall

Fig. 8 Wall heat-flux and wall-adjacent cell y^+ distribution at the channel exit in the case of real fluid obtained with different grid refinements.

Table 4 Grid convergence analysis for wall heat flux computed at the channel exit

	$q_w(z = H/2)$, W/m^2	$q_w(y = 0)$, W/m^2
Coarse grid	235,836	237,351
Medium grid	266,292	253,360
Fine grid	273,264	257,440
Extrapolation	275,334	258,835
Spatial order of accuracy	2.13	1.97

the real fluid density ranges from 45 to 120 kg/m^3. Note that in a single channel section, as the pressure distribution is uniform, the density variation reproduces the isobaric density variation between the minimum and the maximum temperatures of the cross section that are 150 and 300 K. For that reason, in the last channel section, the density variation of the real fluid is more intense in the upper part of the channel (lower temperature) than in the lower part (higher temperature). This behavior is the same as that presented in the state diagram Fig. 2a in which, for a given supercritical pressure, the isochoric lines cluster as temperature reduces.

The different density behavior between perfect gas and real fluid can be easily visualized by means of the compressibility factor plot presented in Fig. 9c. The compressibility factor is a nondimensional parameter that expresses the deviation of a fluid from the perfect gas behavior, and it is defined as

$$Z = \frac{p}{\rho RT} \tag{15}$$

In the case of perfect gas, $Z = 1$. For a supercritical fluid, it is generally less than one (see Fig. 9c). The deviation from the perfect gas case is strong at the inlet section and close to the cold wall where, due to the supercritical thermodynamic behavior, $Z \simeq 0.7$. On the other hand, in the vicinity of the hot wall, the real fluid is a low-density fluid; as a consequence, it behaves almost like a perfect gas and thus $Z \simeq 1$ in the lower part of the channel. The compressibility factor, as a matter of fact, takes into account the density deviation of a real fluid, with respect to the perfect gas model, for a given thermodynamic state (i.e., for a given pressure and temperature). However, the deviation from the perfect gas model is evident in many other thermodynamic variables and transport properties, such as specific heat at constant pressure, thermal conductivity, and viscosity. Their different behavior with respect to the perfect gas models has a direct influence on the heat transfer evaluation between the cooling channel and the working fluid.

The analysis of Fig. 9d clearly shows that the streamwise velocity, for both the perfect gas and the real fluid, is asymmetrically distributed; in fact, the heating from the hot wall implies a greater acceleration of the flow near the bottom wall than near the top wall. Moreover, the shape of the velocity profile in a channel section is similar for both fluids (the perfect gas being faster due to its lower inlet density). In fact, the perfect gas enters the channel with an average velocity of 41 m/s, and the real fluid enters with an average velocity of 31 m/s; the peak velocity value at the channel exit is 74 m/s for the perfect gas and 72 m/s for the real fluid.

The wall heat-flux distribution on the side wall (fin) and the bottom wall at the last channel section, for both the perfect gas and the real fluid, is presented in Fig. 10. At first glance, it is evident that wall heat flux is zero in the proximity of the channel corners. This 3-D effect is due to the enlargement of the boundary layers in that zone. In fact, the sidewall boundary layer and the bottom-wall boundary layer interact with each other in the corner zone, reducing the temperature gradient, and thus wall heat flux, at wall. For this reason, heat flux at the bottom wall presents a maximum value in the symmetry plane (i.e., $y = 0$). Similarly, a maximum value of heat flux occurs on the side wall; this maximum is close to the bottom wall because of the peak velocity

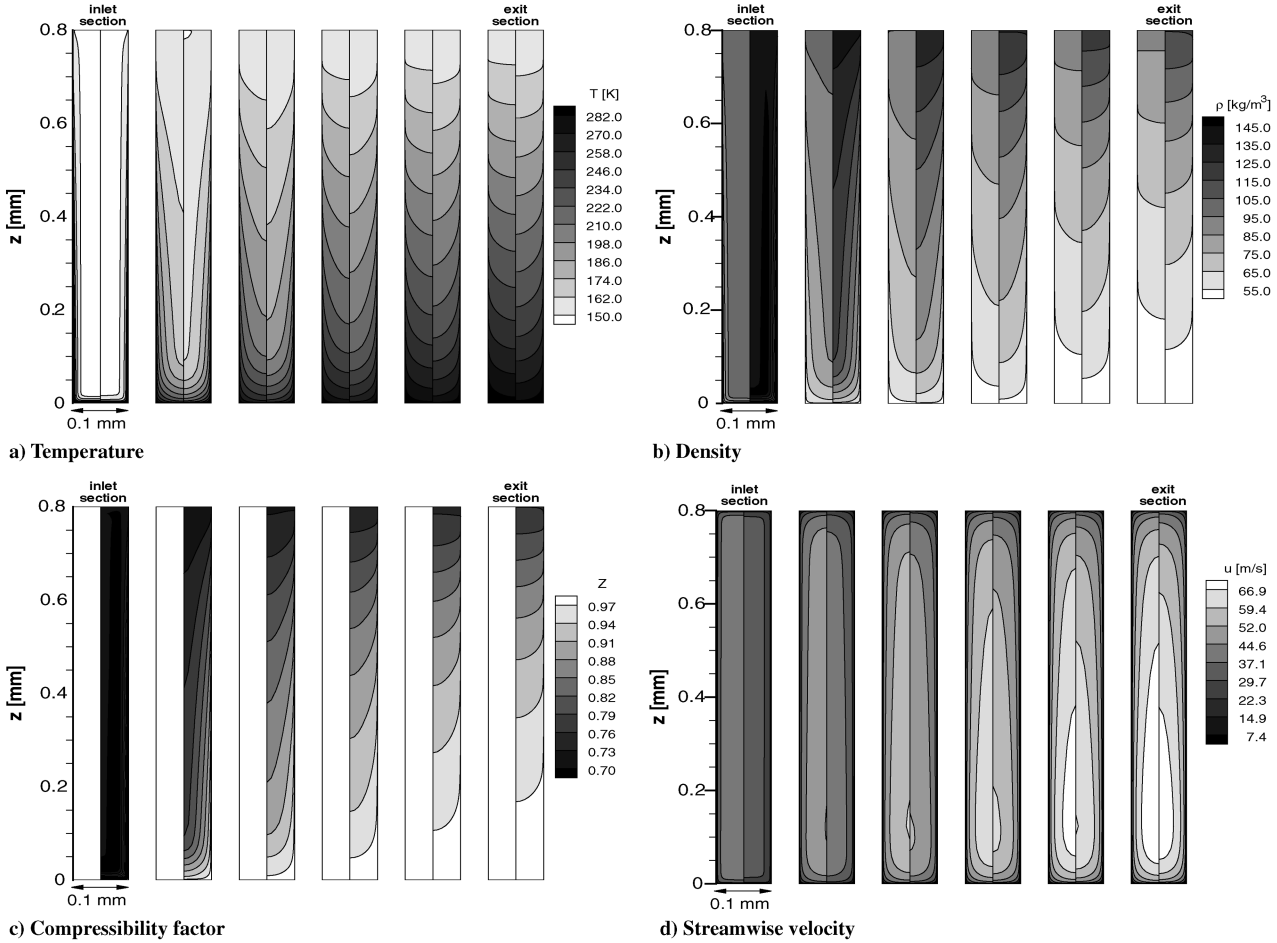

a) Temperature **b) Density**

c) Compressibility factor **d) Streamwise velocity**

Fig. 9 Comparison of the flowfield at various cross sections of the channel for perfect gas (left) and real fluid (right).

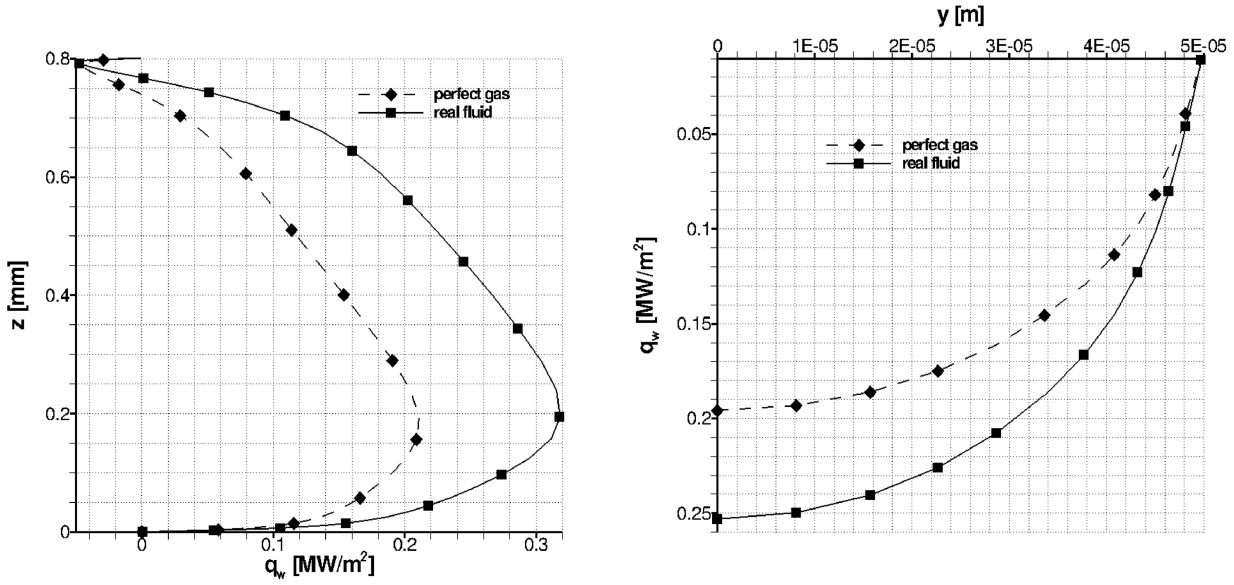

a) Side wall **b) Bottom wall**

Fig. 10 Wall heat-flux distribution at the channel exit for perfect gas and real fluid.

value (see Fig. 9d) in the low-density part of the channel cross section. Note also that, as temperature distribution is imposed at wall, a small amount of heat flux goes from the fluid to the wall in the proximity of the top wall (cold surface).

A further glance at Fig. 10 suggests that the qualitative behavior of wall heat transfer is similar for both perfect gas and real fluid, but in the case of real fluid, the entering heat flux is larger (up to 50%) than in the perfect gas case. Therefore, it is possible to say that the perfect gas model underestimates the cooling efficiency of the fluid. To better quantify this effect, the average heat transfer rate $\dot{Q}$ per unit length of the channel and the mass flow rate $\dot{m}$ of the coolant are presented in Fig. 11a. This parameter is defined by

$$\frac{1}{\dot{m}}\frac{\mathrm{d}\dot{Q}}{\mathrm{d}x} = \frac{1}{\dot{m}}\int_P q_w \,\mathrm{d}P \tag{16}$$

where P is the perimeter of a given channel cross section at the generic streamwise abscissa x. This parameter is of great importance, as it represents the thermal energy Q absorbed by the unit mass m of coolant in the unit length of the channel:

$$\varepsilon = \frac{1}{\dot{m}}\frac{\mathrm{d}\dot{Q}}{\mathrm{d}x} = \frac{1}{m}\frac{\mathrm{d}Q}{\mathrm{d}x} \tag{17}$$

It is possible to consider this parameter as a valid estimation of the coolant efficiency. In Fig. 11a, the area subtended by the curve ε represents the total energy absorbed by the unit mass of coolant along the whole length of the channel. The real fluid absorbs 27% more heat than the perfect gas. Along the channel length, the heat transfer rate regularly decays as the fluid temperature approaches the imposed wall temperature; it is reduced by four times from inlet to exit.

The heat absorbed by the coolant causes its temperature to increase between the channel inlet section and the channel exit section. The bulk temperature increase along the streamwise direction is presented in Fig. 11b for both perfect gas and real fluid. The bulk temperature is defined by

$$T_b = \frac{1}{\dot{m}}\int_A \rho u T \,\mathrm{d}A \tag{18}$$

where A is the channel cross-sectional area. Note that the bulk temperature increase, for both fluids, is larger in the first part of the channel than in the last. This is a direct consequence of the heat transfer decay along the channel length. However, the perfect gas temperature increase is 12% larger than the real fluid increase. The fact that, in the case of perfect gas, temperature increase is larger even if the heat absorbed by the hot walls is lower, is due to the different

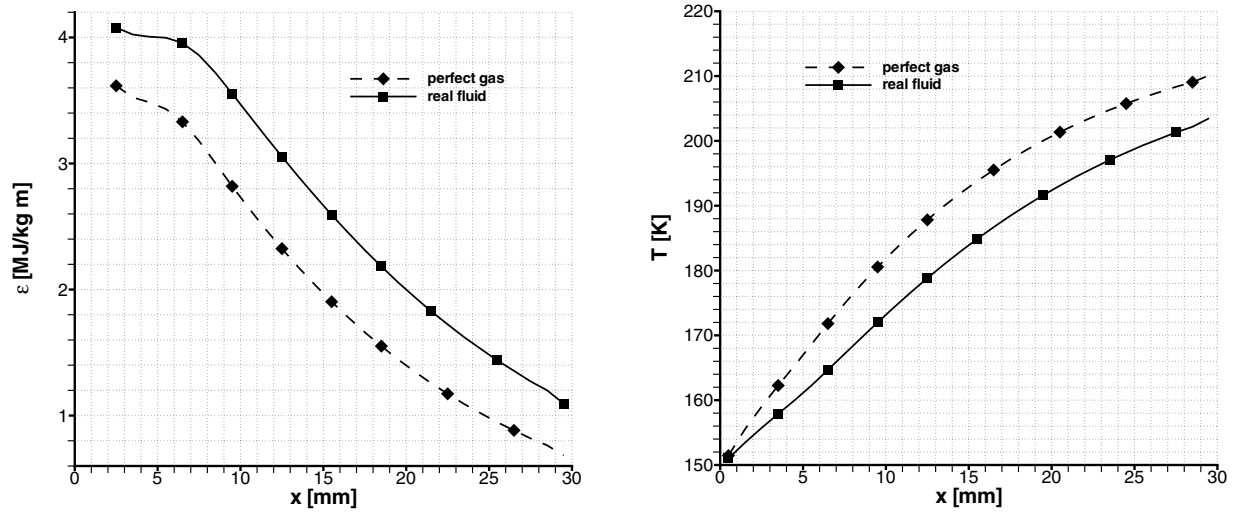

a) Average heat transfer rate **b) Bulk temperature**

Fig. 11 Distribution along the streamwise direction of heat transfer and temperature for perfect gas and real fluid.

specific heat capacity of the two fluids; the constant-value specific heat of calorically perfect gas is almost one half of the specific heat of real fluid in the high-density cold regions. Finally, it is possible to state that the different thermodynamic behavior of the perfect gas model has a direct influence on the cooling capabilities of the fluid; it underestimates the heat transfer rate from the wall to the coolant and overestimates the fluid temperature increase.

VI. Conclusions

A numerical approach to study the supercritical fluid turbulent flow inside the rectangular channels with high-aspect ratio has been presented. Then, a validation for an axisymmetric heated circular-cross-section duct has been carried out by comparison, with experimental data presented in the literature. This comparison has proved that the present code can be used with confidence to study flows with the typical properties of the cooling channel flows: the supercritical behavior of the fluid and high wall heat flux. Then, the validated code has been used to analyze the flow of supercritical nitrogen and treated as a fictitious perfect gas and real fluid inside a 3-D straight channel with a high-aspect ratio. The simulations, verified by grid convergence analysis, have emphasized the different behavior of the perfect gas with respect to the real fluid, and they showed the main 3-D phenomena that occur in such environment: temperature stratification, asymmetric velocity profile, and heat transfer reduction at the channel corners. The heat transfer analysis has shown that the perfect gas model underestimates cooling efficiency; it predicts that heat absorbed by the fluid is roughly 30% less than the value obtained with the real fluid model and that the fluid temperature increase along the channel is roughly 10% larger than the increase predicted by the real fluid simulation.

Acknowledgments

The study has been partially supported by ESA/European Space Research and Technology Center and Ministero dell'Istruzione, dell'Università e della Ricerca (the Italian Ministry of Education, University and Research).

References

[1] Carlile, J. A., and Quentmeyer, R. J., "An Experimental Investigation of High-Aspect-Ratio Cooling Passages," AIAA Paper 92-3154, 1992.

[2] LeBail, F., and Popp, M., "Numerical Analysis of High Aspect Ratio Cooling Passage Flow and Heat Transfer," 29th AIAA/ASME/SAE/ASEE Joint Propulsion Conference, AIAA Paper 1993-1829, June 1993.

[3] Wennerberg, J., Anderson, W., Haberlen, P., Jung, H., and Merkle, C., "Supercritical Flows in High Aspect Ratio Cooling Channels," 41st AIAA/ASME/SAE/ASEE Joint Propulsion Conference, AIAA Paper 2005-4302, July 2005.

[4] Yagley, J., Feng, J., and Merkle, C., "CFD Analyses of Coolant Channel Flowfields," 29th AIAA/ASME/SAE/ASEE Joint Propulsion Conference, AIAA Paper 1993-1830, June 1993.

[5] Yagley, J., Feng, J., Merkle, C., and Lee, Y.-T., "The Effect of Aspect Ratio on the Effectiveness of Combustor Coolant Passages," 28th AIAA/ASME/SAE/ASEE Joint Propulsion Conference, AIAA Paper 1992-3153, July 1992.

[6] Parris, D., and Landrum, D., "Effect of Tube Geometry on Regenerative Cooling Performance," 41st AIAA/ASME/SAE/ASEE Joint Propulsion Conference, AIAA Paper 2005-4301, July 2005.

[7] Wennerberg, J., Jung, H., Schuff, R., Anderson, W., and Merkle, C., "Study of Simulated Fuel Flows in High Aspect Ratio Cooling Channels," 42nd AIAA/ASME/SAE/ASEE Joint Propulsion Conference, AIAA Paper 2006-4708, July 2006.

[8] Jung, H., Merkle, C., Schuff, R., and Anderson, W., "Detailed Flowfield Predictions of Heat Transfer to Supercritical Fluids in High Aspect Ratio Channels," 43rd AIAA/ASME/SAE/ASEE Joint Propulsion Conference, AIAA Paper 2007-5548, 2007.

[9] Merkle, C., Sullivan, J., Buelow, P., and Venkateswaran, S., "Computation of Flows with Arbitrary Equation of State," *AIAA Journal*, Vol. 36, No. 4, 1998, pp. 515–521. doi:10.2514/2.424

[10] Knab, O., Fröhlich, A., Wennerberg, D., and Haslinger, W., "Advanced Cooling Circuit Layout for the VINCI Expander Cycle Thrust Chamber," 38th AIAA/ASME/SAE/ASEE Joint Propulsion Conference, AIAA Paper 2002-4005, July 2002.

[11] Graham, R., Hendricks, R., and Simoneau, R., "Convective Heat Transfer to Low-Temperature Fluids," *Heat Transfer at Low Temperatures*, edited by W. Frost, Plenum, New York, 1974.

[12] Spalart, P., and Allmaras, S., "A One-Equation Turbulence Model for Aerodynamic Flows," *La Recherche Aerospatiale: Bulletin Bimestriel de L'office National D'etudes et de Recherches Aerospatiales*, No. 1, 1994, pp. 5–21.

[13] Müller, S., and Voss, A., "A Riemann Solver for the Euler Equations with Non-Convex Equation of State," Inst. für Geometrie und Praktische Mathematik, TR 168, Aachen, Germany, 1999.

[14] Dahmen, W., Müller, S., and Voss, A., "Riemann Problem for the Euler Equation with Non-Convex Equation of State Including Phase Transitions," *Analysis and Numerics for Conservation Laws*, Springer, Berlin, 2003.

[15] Younglove, B., "Thermophysical Properties of Fluids. I. Argon, Ethylene, Parahydrogen, Nitrogen, Nitrogen Trifluoride, and Oxygen," *Journal of Physical and Chemical Reference Data*, Vol. 11, No. 1, 1982.

[16] Galloüet, T., Herard, J., and Seguin, N., "Some Recent Finite Volume Schemes to Compute Euler Equations Using Real Gas EOS," *International Journal for Numerical Methods in Fluids*, Vol. 39, No. 12, 2002, pp. 1073–1138. doi:10.1002/fld.346

[17] Van Leer, B., "Towards the Ultimate Conservative Difference Scheme. 5: A Second-Order Sequel to Godunov's Method," *Journal of Computational Physics*, Vol. 32, Jul 1979, pp. 101–136. doi:10.1016/0021-9991(79)90145-1

[18] Harten, A., Engquist, B., Osher, S., and Chakravarthy, S., "Uniformly High Order Accurate Non-Oscillatory Schemes, 3," *Journal of Computational Physics*, Vol. 71, No. 2, 1987, pp. 231–303.

[19] Pizzarelli, M., "Modeling of Cooling Channel Flow in Liquid-Propellant Rocket Engines," Ph.D. Thesis, Dept. of Mechanics and Aeronautics, Univ. of Rome "La Sapienza", Rome, 2008.

[20] Toro, E., *Riemann Solvers and Numerical Methods for Fluid Dynamics*, Springer–Verlag, Berlin, 1999.

[21] Glaister, P., "An Approximate Linearised Riemann Solver for the Euler Equations for Real Gases," *Journal of Computational Physics*, Vol. 74, No. 2, 1988, pp. 382–408. doi:10.1016/0021-9991(88)90084-8

[22] Meyer, M. L., "Electrically Heated Tube Investigation of Cooling Channel Geometry Effects," 31st AIAA/ASME/SAE/ASEE Joint Propulsion Conference, AIAA Paper 1995-2500, July 1995.

[23] Roache, P. J., *Verification and Validation in Computational Science and Engineering*, Hermosa, Albuqurerque, NM, 1998.

J. Gore
Associate Editor